# Features of near and far SOL heat fluxes on the Wendelstein 7-X inboard limiters

**H. Niemann[1], M. W. Jakubowski[1], F. Effenberg[2], S. A. Bozhenkov[1], B. Cannas[3], A. Langenberg[1], F.Pisano[3], K. Rahbarnia[1], L. Rudischhauser[1], T. Stange[1], F. Warmer[1], G. A. Wurden[4] and the W7-X Team[1]**

1 Max-Planck-Institut für Plasmaphysik, Wendelsteinstr. 1, 17491 Greifswald, Germany

2 Department of Engineering Physics, University of Wisconsin, Madison, WI 53706, USA

3 University of Cagliari, Cagliari, Italy

4 Los Alamos National Laboratory, PO Box 1663, Los Alamos, NM 87545, USA

E-mail: `Holger.Niemann@ipp.mpg.de`

**Abstract.** The power fall-off length is used as a characteristic dimension to describe the power exhaust in the scrape-off layer in magnetic confinement fusion devices. Measurements from the limiter campaign of the stellarator Wendelstein 7-X with inboard limiters are presented with the first-time characterisation of the limiter heat loads. Two fall-off regimes are found with a narrow near SOL with power fall-off length in millimeters and a wider far SOL with fall-off lengths of several centimeters. An attempt is made to describe both regimes with a scaling law for plasma with different heating powers and densities. The results confirm the major geometry effects of the connection length on the heat transport predicted by 3D modelling.

Submitted to: *Nucl. Fusion*

*Keywords*: W7-X, stellarator, strike line, heat loads, limiter, fall-off length, scrape-off layer, plasma surface interaction

## 1. Introduction

In order to ensure safe operation of present and future fusion devices proper handling of the power exhaust needs to be addressed. Although in tokamaks a poloidal divertor is widely used different design concepts for the plasma facing components as well as magnetic field geometry are studied in tokamaks and stellarators. A narrow region at the plasma edge, where the power leaves the confined plasma region through the last closed flux surface and is deposited along open magnetic flux tubes to the plasma facing components, is called scrape-off layer(SOL). The radial fall-off of the power flux in SOL results from competition between parallel and perpendicular heat transport. Due to the significant difference between parallel and perpendicular heat transport is the typical fall-off length in tokamaks very narrow. This is of particular interest for next step devices, e.g., ITER where a significant amount of power ($P_{SOL}$=80-130 MW for divertor operation in D-T [1],$P_{SOL}$= 3-5 MW[2] for limiter operation) needs to leave the plasma. Therefore many studies of power fall-off length have been performed on different devices.

Typically a shape of power fall-off length function in SOL is described with the help of an exponential decay function.

$$q_{||} = q_0 \exp\left(-\frac{(r - r_{LCFS})}{\lambda_q}\right) \tag{1}$$

with $q_0$ the parallel heat flux at the LCFS and $r_{LCFS}$ the radius of the LCFS.

However, many tokamaks reported that in a case of plasmas limited by an inboard limiter, a second, narrow fall-off length has been found very near to LCFS [3, 4, 5]. In the far SOL, the power fall-off length is reported to be of order of 1-2 centimeters, while in the near SOL it is only a few millimeters. The equation 1 needs to incorporate both SOLs and takes the following form

$$q_{||} = q_n \exp\left(-\frac{(r - r_{LCFS})}{\lambda_{qn}}\right) + q_f \exp\left(-\frac{(r - r_{LCFS})}{\lambda_{qf}}\right) \tag{2}$$

with $\lambda_{qn}$ the narrow fall-off length in the near SOL, $\lambda_{qf}$ the fall-off length of the far SOL and $q_n$, $q_f$ the contributions of both regions to the parallel flux at the LCFS.

The near SOL was measured first at JET[3] with IR thermography and Langmuir probes. As a result, multi-machine studies were triggered to measure the near and far SOL on the inner and outer limiters.

The physics mechanisms leading to the formation of the near SOL is not yet fully understood. At JET a hypothesis was formed that the enhanced inner wall loads may result from funnelling effect (i.e., additional power deposition due to cross-field transport) or possibly as a result of the diffusive attraction of the heat flux at the limiter ridge [3]. Results from TCV[4, 5] and COMPASS[6] showed that non-ambipolar currents correlate with the power entering the near SOL, but their presence alone is not sufficient to explain the enhancement in the heat deposition close to the limiter.

For ITER the plasma start is favoured to be attached mainly to the inner limiters for several reasons [2]. The initial design of the ITER first wall assumed single exponential

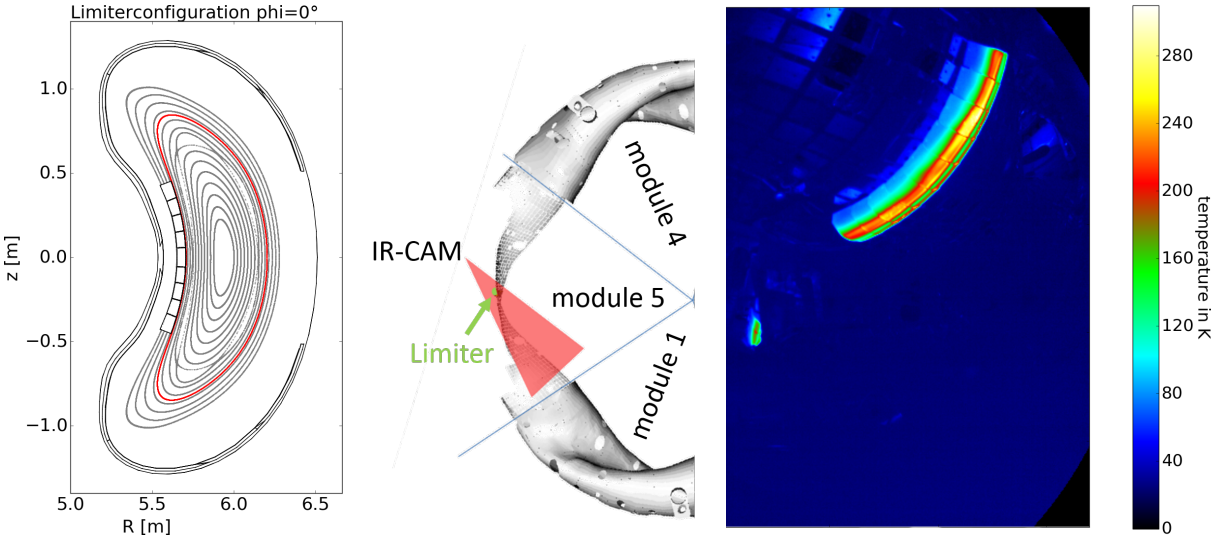


(a) Poincare (b) Top-down view (c) IR view

**Figure 1.** (a) Poincare Plot for vacuum field and ideal coils of the limiter configuration at the bean-shape plane. The LCFS is shown in red, and the nine limiters tiles are visible at the inner side of the machine. (b) Top-down view on the CAD Model of the plasma vessel of Wendelstein 7-X. The machine is structured into five similar modules corresponding to the five-fold symmetry. The sight lines of the radial viewing FLIR and the toroidal viewing DIAS IR camera system are shown in red. The Limiters are shown in green. (c) IR image from the DIAS camera system. The inboard side of W7-X in module 5 with temperature pattern on limiter 5 is visible. Additionally, a reflection on the divertor mounting structure can be seen at the left side.

fall-off length [7, 8]. This assumption was driven by measurements with Langmuir probes in JET, Tore Supra, and DIII-D [2]. The additional narrow channel near the LCFS would raise the heat flux onto the limiter at the apex by a factor of 4 above the expected values. Therefore a design of the ITER first wall has been changed in order to accommodate increase heat flux due to near SOL [2].

In this paper, the results of thermographic observation of inner limiter and the deduced power fall-off length in the first operation phase of Wendelstein 7-X(W7-X) are presented. Up to now, there were no studies of SOL parameters in stellarators apart of LHD [9, 10] and W7-AS [11]. As W7-X in the initial phase operated with five inboard limiters [12, 13], it gave us the possibility to look into the issue of near and far SOL in a large stellarator. The paper is structured in the following way; section 2 introduces W7-X and the infrared systems during limiter campaign. Afterwards, in section 3, measurements and the method to calculate the power fall-off length is described. Section 5 shows the main results and the scaling of the fall-off length with different plasma parameters. In section 6 the results from section 5 are discussed and finally concluded in section 7.

## 2. Experimental set-up

Wendelstein 7-X (W7-X), an advanced stellarator with five-fold symmetry, started its first plasma operation phase (OP 1.1) in December 2015. The five-fold symmetry is represented in the vessel structure with five similar modules (later named module 1 to 5). The inner wall (IW) of the plasma vessel had large surface areas of exposed tiles. Each module was equipped with an uncooled poloidal limiter [13] to protect these areas from plasma contact. The five limiters were located on the inboard, high field side (HFS) of the plasma vessel [14] (figure 1(b)). Each limiter consisting of 9 fine graphite tiles, is specially shaped to be parallel to the magnetic field in the bean-shape plane and designed to handle heat fluxes up to $10 MW/m^2$ [15]. The magnetic field configuration for the limiter phase has been chosen to avoid stochastic regions and large magnetic islands in the scrape-off layer (SOL) (see figure 1(a)). The large islands, which are used in the divertor configurations are pushed inward, into the confined region, to avoid shortcuts in the heat and particle transport towards the wall. This magnetic field assures that the limiters efficiently intercept $> 99\%$ of the convective plasma heat load at the plasma edge. In order to protect parts of the plasma vessel the total injected power per discharge was administratively limited to 4 MJ for machine safety. In OP1.1 electron cyclotron resonance heating (ECRH) was used with power between 4 MW (for up to 1 s) and 0.6 MW ( for up to 6 s). For almost all discharges in OP1.1 toroidal current were very low ($I_{\mathrm{tor}} \leq 2$ kA, see also table 1) and the Shafranov shift was negligible. In such a case a so-called vacuum approach with no plasma response included delivers a valid model for the description of magnetic edge topology. Such an approach will be used throughout the rest of the paper.

In the first campaign, a basic IR observations system with nine near IR (NIR), one mid-wavelength IR (MWIR) and one long-wavelength IR (LWIR) camera were used to measure the surface temperature of the inboard limiters [16]. Figure 1(b) shows a top-down view onto a simplified CAD model of the W7-X inner vessel. The position of the LWIR camera and its view cone is shown in red. The limiters are highlighted in green. The LWIR system contains a modified micro-bolometer camera (8-14 $\mu m$, 50 Hz, 640x480 Pixel) which can operate inside a high magnetic field [17, 18]. The camera was located inside an immersion tube, which was inserted into W7-X between the coils. The camera was observing the left side of all nine tiles of the limiter in module 5 [19](figure 1(c). The other half of the limiter showed similar load pattern following the W7-X symmetry.

Since the data of the NIR cameras suffered from the plasma emission [16] it is excluded from the further analysis. The other MWIR system is also excluded from the analysis due to having only a partial view of the limiter. Because of this the rest of the paper will concentrate on the measurement of the LWIR camera.

## 3. Infrared measurements

### *3.1. Lens distortions and spatial calibration*

The immersion tube set-up [20] was planned to observe the limiters in the first operation phase and the inertially cooled divertors in the upcoming operation phase [18, 16]. Therefore, the LWIR IR camera was equipped with a special wide-angle lens which allows a field of view of 116° x 82° [17]. Together with the large field of view, the wide angle lens also adds strong radial optical distortions into the image. Multiple views of a checkerboard have been used to estimate the intrinsic lens parameter matrix and to correct the strong radial lens distortion for the LWIR camera system. [21]. These parameters are used to map the infrared images onto a simplified CAD Model of the plasma facing components observed by the camera (e.g. limiter, wall panels, vacuum vessel) [21]. From the spatial calibration, a map file, connecting each pixel to a 3D-coordinate inside the machine, is created. This information is then used to determine the real space distance between two pixels.

### *3.2. Emissivity corrections*

In order to properly interpret photon flux measured by an IR camera as surface temperature, it is important to know precisely the emissivity of this surface. Over the course of the campaign, a slow evolution of the physical properties of the limiter surface has been detected. The post-campaign analyses show that the surface changes can be structured into four regions: an outer deposition zone with thin layers of 200 nm to $1\mu m$, a net erosion zone at the strike-line, a prompt re-deposition zone in the strike-line near the center and a smoothed watershed [22]. These changes of the physical properties of the material resulted in local modification of the limiter surface emissivity. The areas of modified emissivity form strike line like patterns which are running poloidally along the limiter. A method for an emissivity correction for all analysed discharges was developed, based on the emissivity measurements in [23]. An example is shown in figure 2. The left and right graph respectively show thermal images of the limiter without and with emissivity correction, taken shortly before the discharge.

The emissivity correction is applied separately to each analysed discharge, to take all surface changes from experiment to experiment into account. The assumption is made that each tile of the limiter is in thermal equilibrium shortly before the discharge. As a result, the surface temperature within each tile should be similar. This assumption implies that the surface temperature variation in the left image of figure 2 is caused by emissivity variations of the surface. Each pixel of a tile is compared to an area within the same tile with known emissivity. The emissivity of each pixel is adjusted until the apparent temperature reaches a similar value or until the emissivity reaches the value of one. The reference area is taken from the middle part of the limiter, where the emissivity was unchanged during the campaign and was equal to 0.82.

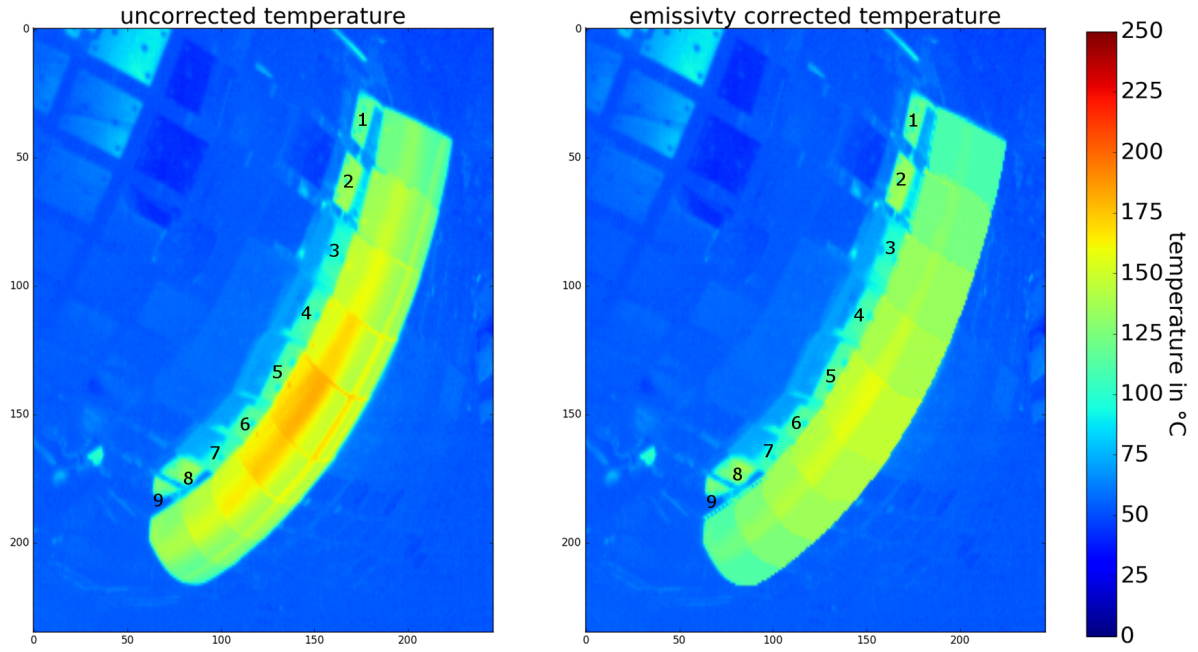


**Figure 2.** The left graph shows an uncorrected infrared image measured shortly before the discharge, the right one shows an emissivity corrected image. In the left image, four different regions can be seen: a deposition zone at the edge of tiles 4,5,6 with a higher emissivity, adjacent the erosion area with unchanged emissivity, near the center the re-deposition zone with higher emissivity. In the very center of the limiter the smoothed region with unchanged emissivity [22, 23]

### *3.3. Heat flux calculation*

After the corrections are applied, each limiter is divided into 450 1D line profiles to cover the surface of all nine tiles. The heat fluxes on the target surfaces are calculated by applying a standard numerical solution of the two-dimensional heat diffusion equations to the evolution of the surface temperature on the investigated area with the THEODOR code [24, 25]. The code numerically solves the equations taking into account temperature dependent material parameters. The two dimensions used here are the depth of the limiter (ignoring its curvature) and the coordinate along the temperature profiles. The gaps between the profiles and the missing pixels are interpolated afterwards to get a full heat flux pattern of the limiter. An example of a heat flux pattern mapped back into the 2D image is shown in figure 3(a).

## 4. Limiter power loads

As presented in Fig. 3 the power loads on the limiter have a shape of two heat stripes, which are running along the length of the limiter separated by the watershed area. Field line tracing (3(b)) and EMC3-EIRENE simulations (3(c) [26]) indicate that the W7-X SOL in OP1.1 consisted of three different helical magnetic flux bundles (indicated as the blue, green and red shape in 3(b)) with limiter-to-limiter connection length of 36 m, 43 m

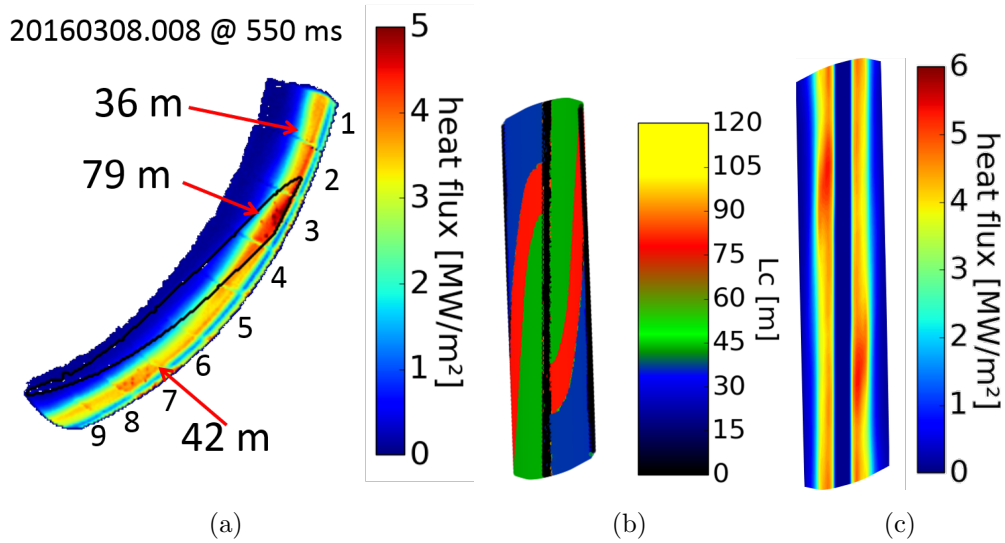


(a) (b) (c)

**Figure 3.** (a) View of the DIAS camera system onto the left side of limiter 5. All nine graphite tiles are visible. The calculated heat flux for a 4 MW discharge is color-coded. The three different flux tube regions are indicated with red arrows and a contour plot for the 79m long flux tube. The dark red spots on tile 3 and 7 are artificial heat flux, caused by the embedded Langmuir probes (b) Pattern of the connection length on the limiter surface from FLT simulation (c) Limiter load from an EMC3 Simulation with P=3.2 MW, $n_e$=8e18 $m^3$, D=1.5 $m^2$/s, 25% energy loss by carbon radiation

and 79 m. These three flux bundles yield heterogeneous power deposition patterns within each of two heat stripes. The maximum of the heat load is located in the region of the flux tube with a connection length of 79 m [26]. The heat transport channel along the flux tubes of different connection lengths can be identified in the power load distributions measured by both cameras [19, 23]. Figure 3(a) shows one example of a power load calculated from the thermographic observation with the LWIR camera. In this graph, the left side of limiter 5 and the left strike-line running down the limiter are shown. A contour plot of the magnetic footprint is overlaid on this figure to indicate the positions of the three flux bundles. Comparing the measured heat flux density with EMC3-Eirene simulation results shows relatively good agreement, i.e. both measurements and modelling resolve three different heat flux channels in the scrape-off layer of limiter plasmas at W7-X.

From the calculated heat flux density $q_{depo}$ the parallel heat flux density $q_{||}$ is calculated using the following relation:

$$q_{depo} = q_{||} \sin(\alpha) \tag{3}$$

The parameter $\alpha$ is the incident angle of the magnetic field to the limiter surface. For the presented measurements, the incident angle is calculated between the field vectors of the magnetic field lines intersecting the limiters and the normal vector of this surface. The field line tracer (FLT) from the W7-X web-service system [27] is used to calculate the magnetic field. It solves the Biot-Savart equation for a given coil and current set. Afterwards, the FLT is used to project the heat flux data from the limiter surface onto

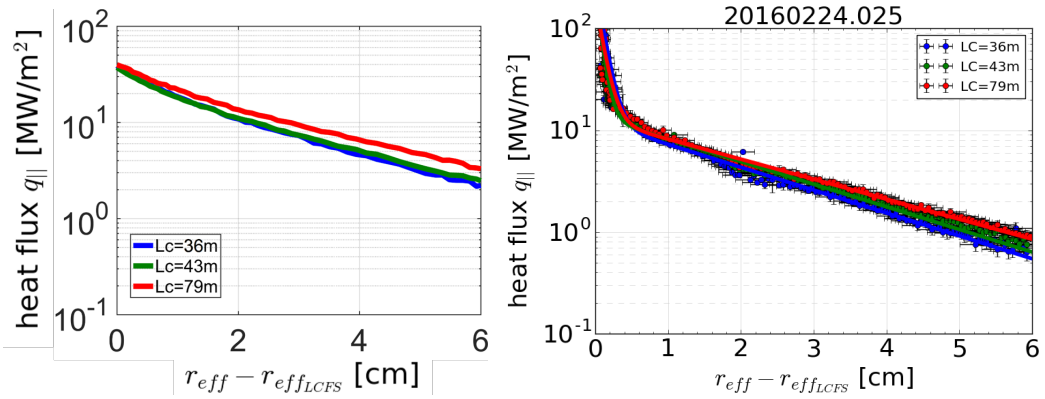


(a) EMC3 (b) IR

**Figure 4.** Profiles from the 3 different fluxtubes for a) EMC3 calculations with P=3.2 MW, $n_e$=8e18 m$^{-3}$, D=1.5 m$^2$/s, 25% energy loss by carbon radiation b) calculated from the IR measurements for the Program 20160224.025 with similar plasma parameters

a plane in order to remove from the analysis effects of the limiter's curvature. Each of the heat flux data points is assigned to a radial coordinate, which is defined as a distance from the last closed flux surface ($r_{\mathrm{eff,LCFS}}$). In such a way 3D heat flux data is simplified to 1D radial profiles of the parallel heat flux $q_{||}(r_{\mathrm{eff}} - r_{\mathrm{eff,LCFS}})$. The effective radius is used to overcome the non-trivial 3D formed plasma shape of W7-X, which goes from a bean-shape plane into a triangular plane and back to a bean-shape plane. It is defined by field lines or by the flux on a magnetic surface:

$$r_{eff} = \int_0^V \frac{dV'}{S(V')} \tag{4}$$

With V as the volume of the flux tube and S(V) the surface of the magnetic surface. For the definition by field lines, used by the FLT, the effective radius is traced out by following the field lines. For each field line, the geometric mean of the distance between points on the field line and the magnetic axis is calculated. The results obtained for three flux tubes with different connection length are presented in Fig. 4. Both experimental data (right) and EMC3-Eirene simulations (left) show increasing fall-off length for flux tubes with longer connection length (see figure 4(a)). The exact dependence will be discussed in Sec. 5.

In order to estimate the error of the parallel heat flux obtained with Eq. 3 an uncertainty of 0.2 MW/m$^2$ for $q_{||\mathrm{depo}}$ is assumed based on measurements after the end of the plasma discharge. The remaining fluctuations around 0 MW/m$^2$ of the heat flux with no plasma contact are taken as a proxy for the error. An error for the calculated value of the incidence angle is obtained by calculating the magnetic field equilibrium with toroidal current between 0 kA and 2 kA. The plasma current is simulated by another coil along the magnetic axis in the FLT. A one-pixel tolerance is used to calculate the spatial uncertainty for the presented data.

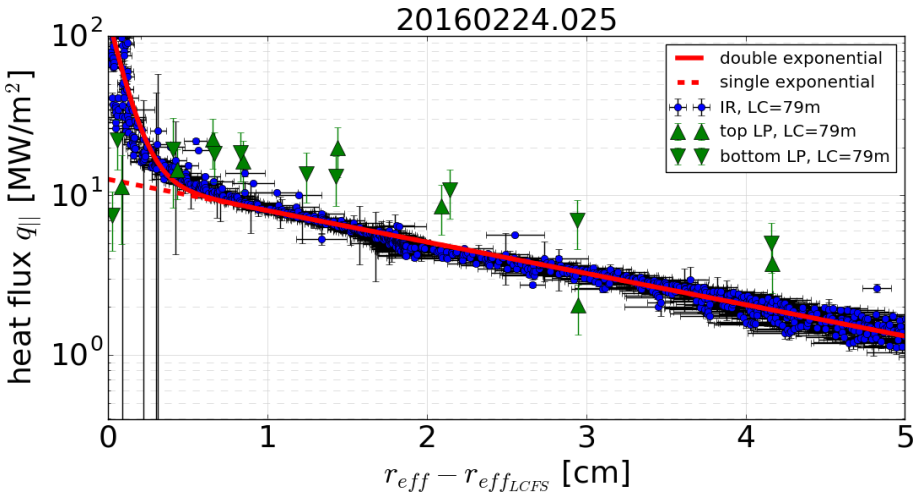


**Figure 5. The radial profile of the parallel heat flux measured for the flux tube with $Lc = 79$ m. The triangles show parallel heat flux measured by the limiter Langmuir probes localized within the same flux tube.**

An exponential decay fit is applied to the radial profiles of the parallel heat flux:

$$q_{||}(r_{\text{eff}}) = q_{||,0} \exp\left(-\frac{(r_{eff} - r_{LCFS})}{\lambda_q}\right) \tag{5}$$

Where $r_{LCFS}$ represents the effective radius of the last closed flux surface, $q_{||,0}$ the heat flux density at the LCFS and $\lambda_q$ the power fall-off length for the parallel heat flux density. In figure 4 such a fit is represented as a dashed line. An exponential fit represents quite well the data only for $r_{\text{eff}} - r_{\text{eff,LCFS}} \geq 0.5$ cm. A double exponential fit function is required to accurately fit the parallel heat flux profile over the whole data range.

$$q_{||}(r_{\text{eff}}) = q_{||,n} \exp\left(-\frac{(r_{\text{eff}} - r_{LCFS})}{\lambda_{qn}}\right) + q_{||,f} \exp\left(-\frac{(r_{\text{eff}} - r_{LCFS})}{\lambda_{qf}}\right) \tag{6}$$

The sum of the $q_{||,n}$ and $q_{||,f}$ represents the parallel heat flux at the LCFS and the parameter $\lambda_{qf}$ and $\lambda_{qn}$ represent the fall-off length for the far and the near SOL. As discussed already in Introduction1 the existence of a near and far SOL when plasma is limited on the inboard limiter has been observed on many tokamaks [3, 2]. An example from Fig. 4 is representative of every discharge in OP1.1, i.e. a double exponential decay of power flux was an inherent feature of limiter discharges at W7-X. It should be noted that due to the presence of $q_{near}$ a significant increase of limiter heat flux is observed for $r_{\text{eff}} - r_{\text{eff,LCFS}}$ close to zero.

Interestingly, the double exponential decay is measured always by an infrared camera and only sometimes by the limiter Langmuir probes [28] (see Fig. 4). The parallel heat

flux to the Langmuir probes is calculated using:

$$\begin{aligned} q_{||,Probe} &= \gamma_t k T_e \Gamma_{||} \\ &= \gamma_t k T_e (1 + \frac{1}{Z}) n_e c_s \\ &= \gamma_t k T_e (1 + \frac{1}{Z}) n_e \sqrt{\frac{k(Z T_e + \gamma_i T_i)}{m_i}} \end{aligned} \tag{7}$$

with $T_i = T_e$, the electron and ion temperature, Z=1.5± 0.5, the average charge of the plasma in front of the probes, $\gamma_t$=2, the heat sheat transmission coefficient, $\gamma_i$=1, the ratio of specific heats for ions, $m_i$ the ion mass (here hydrogen) and $n_e$ the electron density. There are some possible reasons why W7-X limiter Langmuir probes do not measure $q_{||,\mathrm{near}}$:

- The probes closed to the LCFS was recessed a little bit [28] to protect them; therefore they had a low signal and have mainly seen the perpendicular transport
- The probes near $r_{eff} = 0.4cm$ got highly eroded and therefore have unknown collection areas for the flux [28]
- The probes get hot and start to emit electrons, which changes the probe characteristic

Lack of near SOL in W7-X Langmuir probe measurements is in contradiction to COMPASS results with inner wall limiter [6]. However, at W7-X also EMC3-Eirene simulations cannot reproduce the near SOL near the limiter surface. The mechanism, which leads to the formation of near SOL is not included in the models applied in EMC3-Eirene.

## 5. Dependence of radial fall-off length on plasma parameters

To understand better the behaviour of the two different fall-off regimes in W7-X a database of discharges from the limiter operation phase was created. The database contains 13 discharges with a total of 32 data points. Each data point has been selected under the following conditions:

(i) all discharges were conducted with the same magnetic field configuration
(ii) the discharges were conducted in the last month of the campaign with improved wall conditions [29]
(iii) no active impurity seeding
(iv) no ECRH current drive
(v) plasma parameters are almost constant (changes are smaller than 10%) for a time window of 50 ms or more

With good wall conditions are necessary to limit the outgassing of the limiters and the wall, decreasing the radiated fraction and therefore increase the coupling of the limiter with the plasma. The analysed plasma parameters are: the ECRH power $P_{ECRH}$ as input power, the connection length $L_C$ of the different flux tubes, the density $n_e$ and electron

**Table 1.** range of the plasma parameters of the used experiments in the database

| parameter | unit | values | diagnostic |
|---|---|---|---|
| $P_{ECRH}$ | MW | 0.6-4.2 | ECRH bolometer [30] |
| $n_{e_{edge}}$ | $10^{18}m^{-3}$ | 1.7-10 | TS[31] |
| $T_{e_{edge}}$ | keV | 0.02-0.22 | TS[31] |
| $T_{i_{line}}$ | keV | 0.96-1.76 | XICS[32, 33] |
| $I$ | kA | 0.16-1.97 | Rogowski coil [34] |
| $W_{dia}$ | kJ | 5.6-234.6 | diamagnetic loops[34] |
| $P_{lim}$ | MW | 0.18-1.6 | IR camera[17, 19] |
| $f_{loss}$ | % | 47-79 | eq. 8 |
| $L_c$ | m | 36,42,79 | FLT[27] |

temperature $T_e$ measured by the Thomsen scattering (TS) 1.3 cm away from the LCFS, the toroidal current I, the ion temperature measured by the X-ray imaging spectrometer (XICS), the load on the limiters $P_{lim}$ and the loss fraction $f_{loss}$, which covers the energy losses like radiation, fast particle and charge exchange losses. The loss fraction is defined as:

$$f_{loss} = \frac{P_{ECRH} - P_{Lim}}{P_{ECRH}} \tag{8}$$

The load on the limiters are calculated by integrating all taken heat flux profiles along the profiles and in poloidal direction. Since only the left half of one limiter is observed, the integration is scaled up to the full machine using the stellarator symmetry for the other half of the limiter and thermo couple information to know the load ratio between the five limiters. The thermo couples measured the temperature at the back side of each limiter and the temperature increase over a experiment represents the integrated load to this limiter. The load asymmetry can be calculated from the different in the temperature rise. This leads to an asymmetry or up-scaling factor of 4.88 for the load from Limiter 5 to all limiters, because limiter 5 received a little more than the mean load [23].

The range of the different parameters is summarised in table 1 and some example scaling behaviours are shown in figure 6. In order to investigate the influence of the connection length LC on the fall-off length $\lambda_q$ the influences of other plasma parameters are removed by choosing very similar discharges with small variations of heating power (1.5 to 2.5 MW) (left plots in figure 6. For the other six plots, only the fall-off length values for the most extended flux tube are shown. The far fall-off length increases with the connection length and decreases with the input power and density. In case of the near SOL fall-off length, the scaling is rather weak. The dependency on connection length, input power, and density is not explicit, but it decreases with the electron temperature.

To investigate more parameters and to find correlated parameters, a correlation analysis is performed onto the database. The correlation between measured parameters

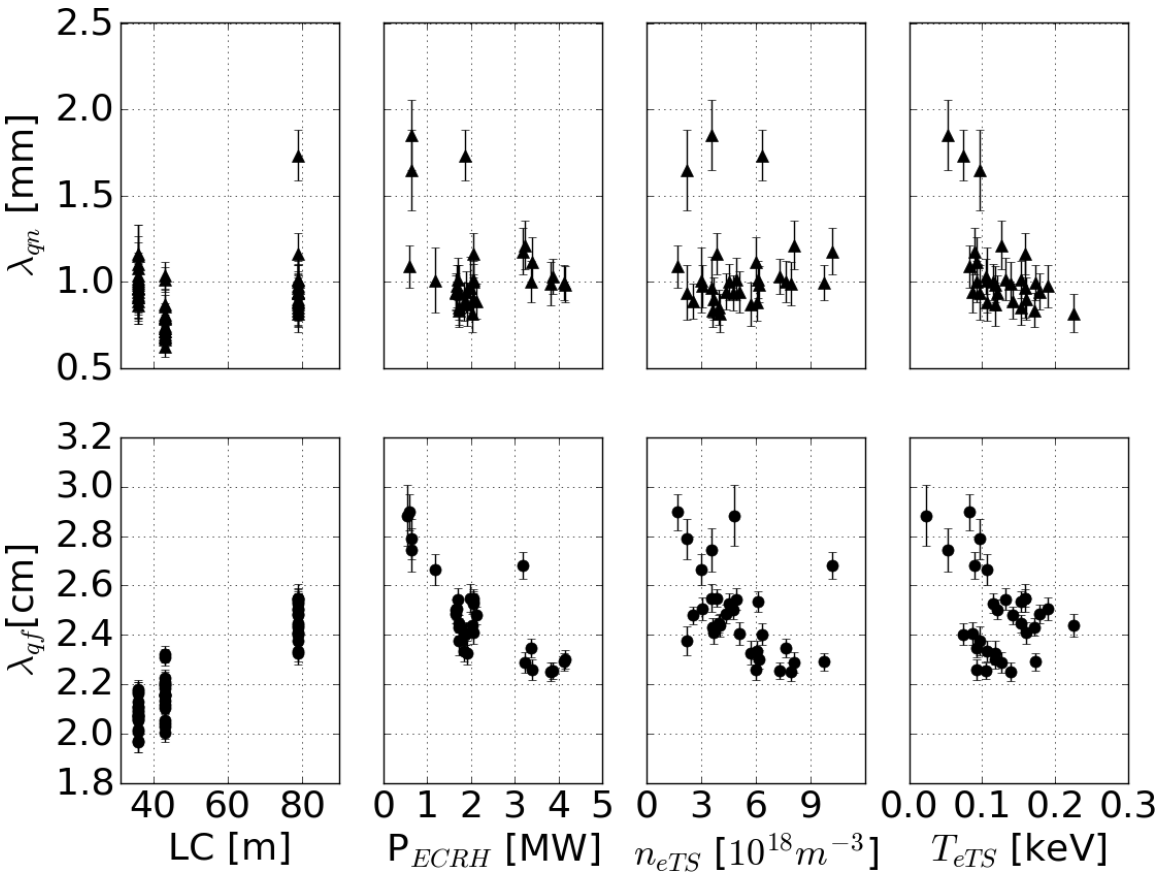


**Figure 6.** dependencies of the fall-off length for near and far SOL on different measured plasma parameters in the limiter campaign of Wendelstein 7-X. The plots against connection length are filtered for input powers between 1.5 and 2.5 MW to limit the scattering. In the remaining plots only the power fall-off length values for the flux tube with a connection length of 79 m are shown.

are calculated in the following form:

$$r_{XY} = \frac{\sum_{i=1}^{N}(X_i - \overline{X}) * (Y_i - \overline{Y})}{(N-1) * s_x * s_y} \tag{9}$$

With N being the number of measurements, X, Y two different parameters from the database, $\overline{X}$, $\overline{Y}$ are the mean of the parameters and $s_X$, $s_y$ are the corrected standard deviations of parameters. The results are shown in table 2. Each combination of parameters in this table represents the correlation between the two parameters. Everything above 50% or below -50% can be seen as not independent and is therefore written in bold numbers. One thing to point out here, is the strong correlation between input power and density, meaning that if the input power is increased, the density is also increased and vice versa. The nearly linear behaviour between density and input power is caused by density restrictions to avoid radiative collapses, meaning that the input power was doubled, if the target density was doubled. This table is also used to identify parameters which show a scaling with the measured power fall-off lengths and heat flux density at the LCFS for the near and far SOL. For the fall-off length in the far

**Table 2.** correlation between the different measured plasma parameters and magnetic field constants. Correlations over 50% are written in bold numbers

| cor.% | $n_{edge}$ | $T_{eedge}$ | $T_i$ | I | $W_{dia}$ | $P_{lim}$ | $f_{loss}$ | $L_C$ | time | $\lambda_{qn}$ | $\lambda_{qf}$ | $q_n$ | $q_f$ |
|---|---|---|---|---|---|---|---|---|---|---|---|---|---|
| $P_{ECRH}$ | **77** | 21 | -44 | -47 | **79** | **88** | 37 | 0 | -36 | -43 | **-55** | **82** | **93** |
| $n_{edge}$ | | -8 | -8 | -41 | **78** | **65** | 46 | 0 | -32 | -14 | -37 | 48 | **60** |
| $T_{eedge}$ | | | -34 | -29 | 22 | 36 | -21 | 0 | -22 | **-56** | -25 | 35 | 35 |
| $T_i$ | | | | 3 | 0 | -34 | -18 | 0 | 15 | 27 | 29 | **-50** | -47 |
| $I$ | | | | | **-52** | -37 | -45 | 0 | **76** | 12 | 36 | -33 | -38 |
| $W_{dia}$ | | | | | | **71** | 35 | 0 | -41 | -36 | -48 | **57** | **72** |
| $P_{lim}$ | | | | | | | -5 | 0 | -24 | -45 | -48 | **78** | **93** |
| $f_{loss}$ | | | | | | | | 0 | **-55** | 0 | -34 | 11 | 12 |
| $L_C$ | | | | | | | | | 0 | 3 | **65** | 18 | 7 |
| $time$ | | | | | | | | | | 15 | 45 | -23 | -28 |

SOL, the parameters with the highest correlation are the input power P, the diamagnetic energy, the load on the limiter, the connection length and the time. Latter is a proxy for different parameters as plasma current, impurity concentration, radiative losses and other unresolved parameters which are changing in time. For the near SOL power fall-off length, the highest correlation has been found for the electron temperature near the LCFS, followed by the load on limiters. All other parameters in the table show a rather weak dependency. The parameters with the highest correlation for the fractions of heat flux densities at the LCFS ($q_n$ and $q_f$) are the input power, power to the limiters, density, and ion temperature and electron temperature.

To find a scaling a fit function in the form of a power law is used in the following form:

$$\lambda_q = c \prod_{i=1}^{n} A_i^{e_i} \tag{10}$$

With c being a factor for unresolved parameters, $A_i$ the plasma parameter, $e_i$ the fitting parameter, the exponent for the plasma parameter and n the number of included plasma parameters. The fitting of the scaling law to the data in the database is performed in the logarithmic polynomial form to linearise the fitting equation:

$$\log \lambda_q = \log c + \sum_{i=1}^{n} e_i * \log A_i \tag{11}$$

In this way the multiple regression model can be applied to determine the quality of the fit. A scan for each plasma parameter has been performed, including a combination of parameters up to a number of three parameters. For both regions in the SOL, the regression model is applied separately with different combinations of input parameters, with the restriction to avoid cross-correlated parameters. The coefficient of determination ($R^2$) and the reduced chi-square ($\chi^2/dof$) are calculated to test and compare the quality of the different fits. Latter includes the number of freedom and the assumptions for the

**Table 3.** results of the fitting for the power fall-off length in the far SOL $\lambda_{qf}$ in cm

| Reg. | Const. | $P_{ECRH}$ | n | $T_{e_{edge}}$ | $L_C$ | $P_{lim}$ | $f_{loss}$ | $\chi^2$/dof | $R^2$ |
|---|---|---|---|---|---|---|---|---|---|
| 1 | 1.04(2) | -0.114(5) | - | - | 0.22(1) | | - | 4.19 | 0.81 |
| 2 | 0.92(2) | - | - | - | 0.22(1) | -0.09(1) | - | 6.73 | 0.71 |
| 3 | 0.98(3) | -0.10(1) | - | - | 0.22(1) | - | -0.12(2) | 3.85 | 0.83 |
| 4 | 0.80(2) | - | - | - | 0.22(1) | -0.10(1) | -0.33(2) | 3.80 | 0.83 |

**Table 4.** results of the fitting for the power fall-off length in the near SOL $\lambda_{qn}$ in mm

| Reg. | Const. | $P_{ECRH}$ | n | $T_{e_{edge}}$ | $L_C$ | $P_{lim}$ | $T_i$ | $\chi^2$/dof | $R^2$ |
|---|---|---|---|---|---|---|---|---|---|
| 1 | 0.41(3) | -0.21(2) | - | -0.46(3) | - | - | - | 5.15 | 0.54 |
| 2 | 0.35(2) | - | - | -0.43(3) | - | -0.21(3) | - | 5.35 | 0.52 |
| 3 | 0.24(2) | - | - | -0.58(3) | - | - | 0.49(8) | 5.41 | 0.52 |
| 4 | 0.30(2) | - | - | -0.45(3) | - | -0.21(3) | 0.35(8) | 5.16 | 0.58 |
| 5 | 0.36(3) | -0.23(3) | - | -0.49(3) | - | - | 0.25(8) | 4.83 | 0.60 |

error. The values to fit for the measured fall-off length in the far SOL reaches from 1.82 cm for the shortest connection length flux tube up to 2.9 cm for the long connection length flux tube. Table 3 shows the four best fitting function for the power fall-off length in the far SOL, which has been found during the analysis. The error for each parameter is shown in the brackets, where the digits in the brackets represent the error of the last digits. The connection length can be combined with any of the other parameters, because it is unrelated to the rest of the plasma parameters (see table 2). The input power cannot be combined with density, the diamagnetic energy or the load on the limiter due to it high correlation (77%, 79% and 88%). The loss fraction is also not independent on the input power, but is nearly independent from the limiter loads. This is also the reason for the strong variation of the exponent for the loss fraction in regression 3 and 4. The combination of limiter power, connection length and loss fraction into the fit gives the best representation of the fall-off length for the given data-set, which reaches a coefficient of determination of 83%. A density dependence has not been found, due to its strong correlation with the input power. The resulting found scaling law for the fall-off length in the far SOL is therefore given by:

$$\lambda_{qf}[cm] = (0.79 \pm 0.02) L_C^{0.22\pm0.01}[m] P_{lim}^{-0.10\pm0.01}[MW] f_{loss}^{-0.34\pm0.02} \tag{12}$$

and is visualized in figure 7(b). The analysis is repeated for the data of the near SOL in a similar way. For the near SOL the measured power fall-off length ranges from 0.6 mm up to 3.6 mm. The respectively larger error bars have to be taken into account in the fit. The error is larger, due to resolution limitations of the DIAS view, in this small region. The main findings are summarized in table 4. Since the electron temperature showed the highest correlation value for the near SOL power fall-off length it is used in all presented regressions. The line integrated ion temperature is one of the few parameters, which have

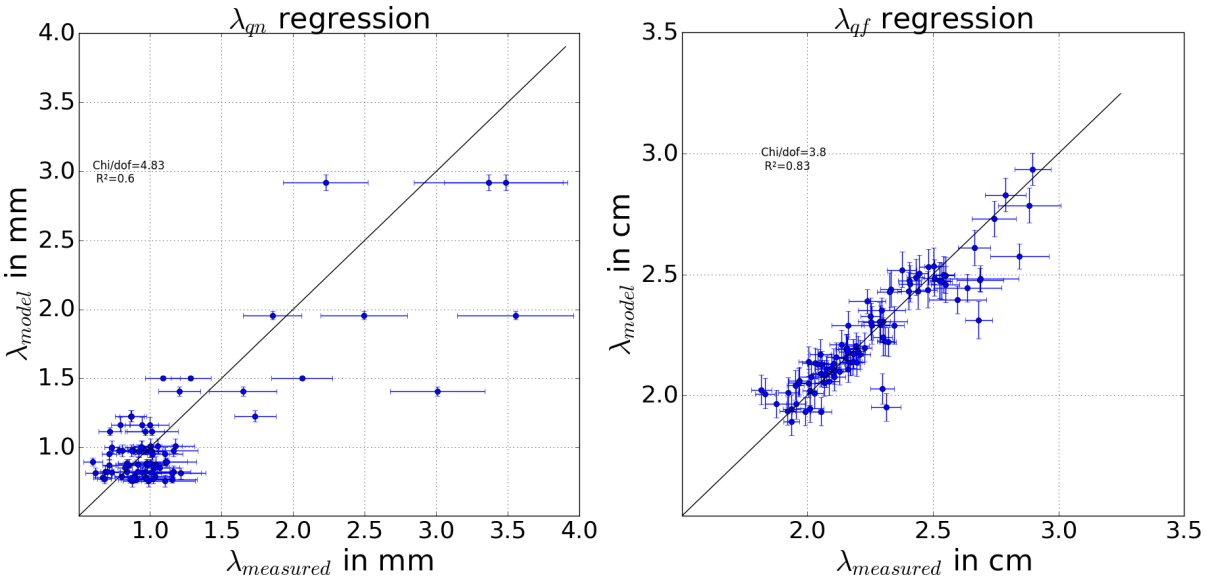


(a) regression result for the near SOL

(b) regression result for the far SOL

**Figure 7.** the two found regression models plotted against the measured values for the power fall-off length.

a positive scaling with the fall-off length and the effects of input power or load on the limiters are also much weaker than in the far SOL scaling. The best found power law for the near SOL is given by electron, ion temperature and connection length:

$$\lambda_{qn}[mm] = 0.36 \pm 0.03 P_{ECRH}^{-0.23\pm0.03} T_i^{0.25\pm0.08} T_e^{-0.49\pm0.03} \tag{13}$$

This fit reaches a good reduced chi square value of 4.83 but only a coefficient of determination of 60%. This result implies that not all parameters have been found, which has an effect on the fall-off length. Figure 7(a) visualizes this result including the error bars. The majority of the measured values of $\lambda_q n$ are a group of values with less than 1.5 mm. This values are at the limit of the camera resolution after the projection into the plane. A similar analysis can be repeated for the parallel heat flux densities at the LCFS. The values for the fraction from near SOL reaches from 1.8 MW/m$^2$ to 391.8 MW/m$^2$ and the fraction from the the far SOL for reaches from 1.3 MW/m$^2$ to 22 MW/m$^2$ From table 2 the parameters with the highest influence are input power, density, ion temperature, diamagnetic energy and the limiter load. The majority of these parameters are strongly correlated with the input power, which has the highest influence. The found scaling for the heat flux densities are:

$$q_n[MW/m^2] = (215.55 \pm 13.43) * P_{ECRH}^{1.55\pm0.02} * T_e^{0.98\pm0.02} (R^2 = 85\%) \tag{14}$$

$$q_f[MW/m^2] = (8.65 \pm 0.07) * P_{ECRH}^{0.975\pm0.003} * T_e^{0.281\pm0.004} (R^2 = 93\%) \tag{15}$$

These results are shown in figure 8. The results show, that the found near SOL channel contains a high fraction of the SOL energy ($P_{SOL}$) in a small volume around the LCFS.

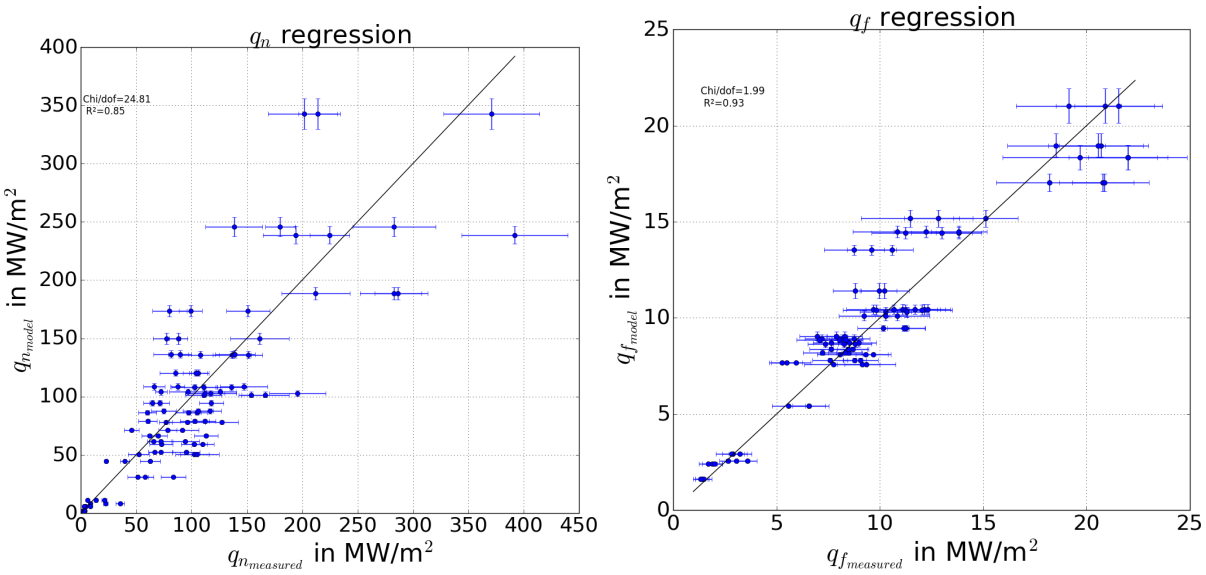


(a) regression result for the near SOL

(b) regression result for the far SOL

**Figure 8.** the two found regression models plotted against the measured values for the heat flux densities close to the LCFS.

To investigate the part of the near SOL, the SOL energy $P_{SOL}$ has to be computed for the W7-X geometry. Since the symmetry approximations from tokamaks do not apply here, the SOL energy is computed by the parallel heat flux profiles and the area which is covered by the flux tubes:

$$\begin{aligned} P_{SOL} &= \sum_{i=1}^{\#Limiter} \sum_{j=1}^{\#flux\,tube\,types} L_{pol_j} \frac{B_\theta}{B_\phi} \int_0^{r_{wall}} 2q_{ij}(r'_{eff})\,\mathrm{d}r'_{eff} \\ &\approx S_L \frac{B_\theta}{B_\phi} \sum_{j=1}^{3} \theta_j r_{eff_{wall}} (q_{n_j} * \lambda_{qn_j} + q_{f_j} * \lambda_{qf_j}) \end{aligned} \tag{16}$$

The sum over the limiters covers the complete area of the SOL. The factor two counts for the left and right side of the limiter. The second sum covers the presence of the different flux tubes with different connection length. $L_{pol_j}$ are the poloidal length of a flux tube and the factor $B_\theta/B_\phi$ tilts the projected plane into the field direction. The Sum over all limiters is approximated with the symmetry factor $S_L$ to work with the measurement of one limiter. It will be five if all limiters get the same load. As described before, the limiter load was not fully symmetric so, that the asymmetry factor of 4.88 is used here again. $\theta_j$ is the poloidal angle range of the flux tube j and $r_{reff_{wall}}$ is the effective radius of the outermost flux surface (see the outermost, by limiter intersected flux surface in figure

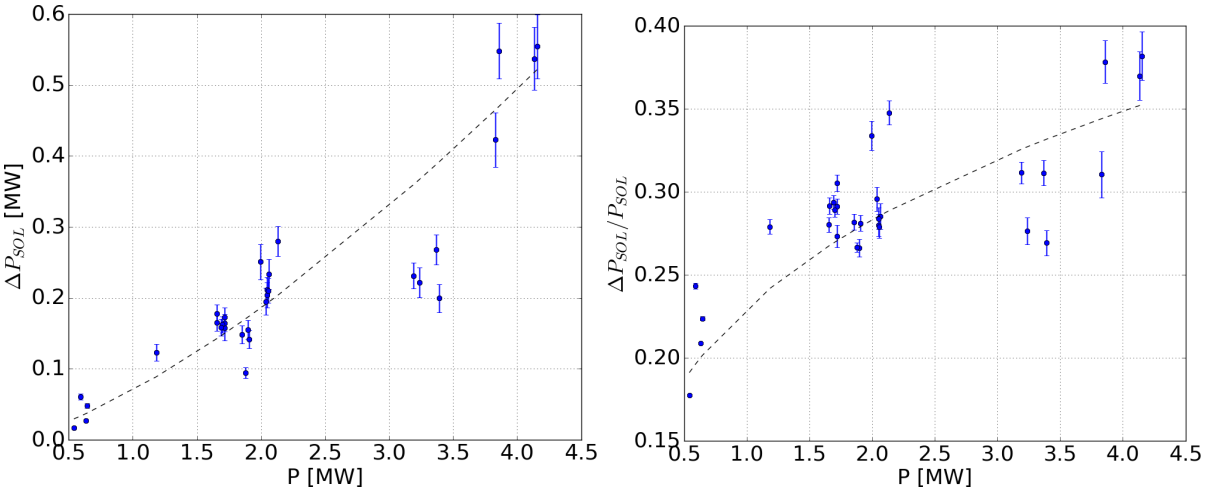


(a) additional near $P_{SOL}$ energy (b) relative fraction of the near SOL energy

**Figure 9.** Power added by the near SOL in absolute and relative to the total Power in the SOL

1(a)). Similarly the additional near SOL energy is calculated:

$$\begin{aligned}\Delta P_{SOL} &= \sum_{i=1}^{\#Limiter} \sum_{j=1}^{\#flux\,tube\,tupes} L_{pol_j} \frac{B_\theta}{B_\phi} \int_0^{r_{wall}} 2(q_{ij}(r'_{eff}) - q_{ij_f}(r'_{eff}))\,\mathrm{d}r'_{eff} \\ &\approx S_L \frac{B_\theta}{B_\phi} \sum_{j=1}^{3} \theta_j r_{eff_{wall}} (q_{n_j} * \lambda_{qn_j})\end{aligned} \tag{17}$$

The results for the power in the near SOL are summarised in figure 9. It reaches from 17 kW to 554 kW, meaning that this near SOL carries between 17% and 38% of the total SOL power. With increasing input power the power in the near SOL increases more than linear, resulting in a higher fraction of energy in the near SOL with increasing heating power.

## 6. Discussion

The calculated scaling laws for the power fall-off length of the near and far SOL show no dependency on the density. Other studies on tokamaks show on the other hand a clear dependency of the near and far SOL power fall-off length on the density [5]. This effect has not been seen in the data-set of W7-X, although EMC3-Eirene calculations show a clear dependency of the far SOL fall-off length on the density (figure 10). The reason for this is probably the strong coupling of the density with the input power, which suppresses the effect of the density. The found positive scaling of the main SOL with connection length is qualitatively in agreement with the EMC3-Eirene scaling, which is given by:

$$\lambda_q \sim \sqrt{D * L_C} \sim D^{0.5} L_C^{0.5} \tag{18}$$

With D being the diffusion coefficient. However, the measurements show a factor two lower scaling factor. The factor can differ due to a change of the anomalous diffusion.

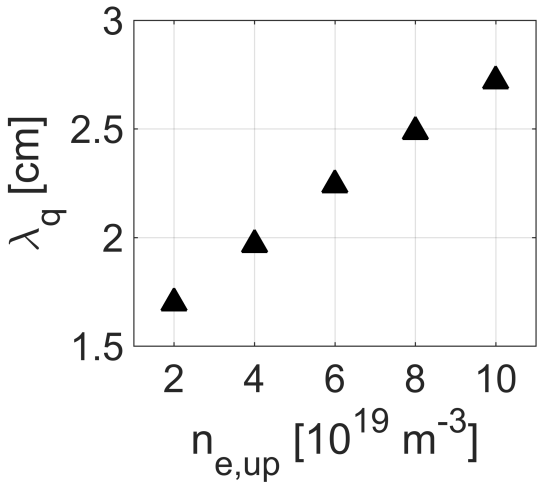


**Figure 10.** power fall-off length from EMC3-Eirene for different up-stream densities. P=3.2 MW, D=1.5 $m^2/s$

The effect of the anomalous diffusion was not investigated due to missing measurements of this quantity. Also, the strong relation with the plasma current in tokamaks has not been seen in W7-X, since the plasma current is two orders of magnitude smaller in a stellarator. In tokamaks, the scaling for the fall-off length depends strongly on the plasma current $I_p$ and therefore on the poloidal field $B_p$ [35]. The current effect in a tokamak can be separated into a heating component $P_{in}$ and a poloidal field component $B_p$ for the scaling. The latter is related to the connection length $L_c$. The connection length $L_c$ decreases with increasing poloidal field $B_p$ because the field lines twist get stronger in cylindrical limiter plasma. This lead to the following relation:

$$\lambda_q \sim \frac{1}{{I_p}^a} \sim \frac{1}{{P_{in}}^b * {B_p}^c} \sim \frac{{L_C}^d}{{P_{in}}^b} \tag{19}$$

With a,b,c and d as the scaling factors. This relation shows the agreement between the presented results and the tokamak research for the far fall-off length. The results and scaling for the near SOL have to be taken with caution because the system resolution limits the accuracy of the values and the found scaling has still a big scatter.

## 7. Conclusion

In this paper, the first measurements of the power fall-off length in the limiter phase of the advanced stellarator Wendelstein 7-X have been presented. It was shown that two different fall-off regimes were measured for the inner wall limiter configuration: a near SOL and a far SOL, similar to the measurements on tokamaks for inboard limiters. The measured power fall-off length in the near SOL reaches from 0.6(5) mm up to 3.6(5) mm and is in the far SOL a magnitude larger with values from 18.2(5) mm to 29.0(5) mm. The effect of the wall to wall connection length together with loads to the limiter as a proxy for the power in the SOL have been shown as main parameters, which are affecting

the far fall-off length. A qualitative agreement with EMC3-Eirene modelling for the main SOL scaling with connection length was shown. For the near SOL, it was shown that the electron temperature near the last closed flux surface plays a dominant role in the behaviour of this narrow regime. It has also been shown that this near SOL regime contains up to 38% of the power in the SOL. It is not covered by 3D-Modelling, due to a missing physics model for the formation of this near SOL feature.

## Acknowledgments

This work has been carried out within the framework of the EUROfusion Consortium and has received funding from the Euratom research and training program 2014-2018 and 2019-2020 under grant agreement No 633053. The views and opinions expressed herein do not necessarily reflect those of the European Commission. This work was supported in part by the U.S. Department of Energy (DoE) under grant DE-SC0014210 and by discretional funding of the Department of Engineering Physics and the College of Nuclear Engineering at the University of Wisconsin - Madison, USA.

## References

[1] A. Loarte, B. Lipschultz, A. Kukushkin, G. Matthews, P. Stangeby, N. Asakura, G. Counsell, G. Federici, A. Kallenbach, K. Krieger, A. Mahdavi, V. Philipps, D. Reiter, J. Roth, J. Strachan, D. Whyte, R. Doerner, T. Eich, W. Fundamenski, A. Herrmann, M. Fenstermacher, P. Ghendrih, M. Groth, A. Kirschner, S. Konoshima, B. LaBombard, P. Lang, A. Leonard, P. Monier-Garbet, R. Neu, H. Pacher, B. Pegourie, R. Pitts, S. Takamura, J. Terry, E. Tsitrone, the ITPA Scrape-off Layer, D. Group, Chapter 4: Power and particle control, Nuclear Fusion 47 (6) (2007) S203–S263. doi:10.1088/0029-5515/47/6/s04.
URL https://doi.org/10.1088%2F0029-5515%2F47%2F6%2Fs04

[2] M. Kocan, R. Pitts, G. Arnoux, I. Balboa, P. de Vries, R. Dejarnac, I. Furno, R. Goldston, Y. Gribov, J. Horacek, M. Komm, B. Labit, B. LaBombard, R. Lasnier, C.J.and Mitteau, F. Nespoli, D. Pace, R. Panek, P. Stangeby, J. Terry, C. Tsui, P. Vondracek, Impact of a narrow limiter SOL heat flux channel on the ITER first wall panel shaping, Nuclear Fusion 55 (2015) 033019.

[3] G. Arnoux, T. Farley, C. Silva, S. Devaux, M. Firdaouss, D. Frigione, R. Goldston, J. Gunn, J. Horacek, S. Jachmich, P. Lomas, S. Marsen, G. Matthews, R. Pitts, M. Stamp, P. Stangeby, JET-EFDA Contributors, Scrape-off layer properties of ITER-like limiter start-up plasmas in JET, Nuclear Fusion 53 (2013) 073016.

[4] F.Nespoli, B.Labit, I.Furno, G.P.Canal, A.Fasoli, the TCV team, Heat loads in inboard limited L-mode plasmas in TCV, Journal of Nuclear Materials 463 (2015) 393–396. doi:https://doi.org/10.1016/j.jnucmat.2014.11.137.

[5] F. Nespoli, B. Labit, I. Furno, J. Horacek, C. Tsui, J. Boedo, R. Maurizio, H. Reimerdes, C. Theiler, P. Ricci, F. Halpern, U. Sheikh, K. Verhaegh, R. Pitts, F. Militello, T. E. M. Team, T. T. Team, Understanding and suppressing the near scrape-off layer heat flux feature in inboard-limited plasmas in tcv, Nuclear Fusion 57 (12) (2017) 126029.
URL http://stacks.iop.org/0029-5515/57/i=12/a=126029

[6] J. Horacek, P. Vondracek, R. Panek, R. Dejarnac, M. Komm, R. Pitts, R. Goldston, P. Stangeby, E. Gauthier, P. Hacek, J. Havlicek, M. Hron, M. Imrisek, F. Janky, J. Seidl, Narrow heat flux channels in the COMPASS limiter scrape-off layer, Journal of Nuclear Materials 463 (2015) 385–388.

[7] P. Stangeby, R. Mitteau, Analysis for shaping the iter first wall, Journal of Nuclear Materials 390-391 (2009) 963 – 966, proceedings of the 18th International Conference on Plasma-Surface Interactions in Controlled Fusion Device. doi:https://doi.org/10.1016/j.jnucmat.2009.01.249.
URL http://www.sciencedirect.com/science/article/pii/S0022311509002748

[8] R. Mitteau, P. Stangeby, C. Lowry, M. Merola, Heat loads and shape design of the iter first wall, Fusion Engineering and Design 85 (10) (2010) 2049 – 2053, proceedings of the Ninth International Symposium on Fusion Nuclear Technology. doi:https://doi.org/10.1016/j.fusengdes.2010.07.022.
URL http://www.sciencedirect.com/science/article/pii/S092037961000342X

[9] S. Masuzaki, T. Morisaki, N. Ohyabu, A. Komori, H. Suzuki, N. Noda, Y. Kubota, R. Sakamoto, K. Narihara, K. Kawahata, K. Tanaka, T. Tokuzawa, S. Morita, M. Goto, M. Osakabe, T. Watanabe, Y. Matsumoto, O. Motojima, the LHD Experimental group, The divertor plasma characteristics in the large helical device, Nuclear Fusion 42 (6) (2002) 750–758. doi:10.1088/0029-5515/42/6/313.
URL https://doi.org/10.1088%2F0029-5515%2F42%2F6%2F313

[10] S. Masuzaki, T. Morisaki, M. Shoji, Y. Kubota, T. Watanabe, M. Kobayashi, J. Miyazawa, M. Goto, S. Morita, B. J. Peterson, N. Ohyabu, A. Komori, O. Motojima, L. E. Group, H. Ogawa, Overview and future plan of helical divertor study in the large helical device, Fusion Science and Technology 50 (3) (2006) 361–371. arXiv:https://doi.org/10.13182/FST06-A1257, doi:10.13182/FST06-A1257.
URL https://doi.org/10.13182/FST06-A1257

[11] M. Hirsch, J. Baldzuhn, C. Beidler, R. Brakel, R. Burhenn, A. Dinklage, H. Ehmler, M. Endler, V. Erckmann, Y. Feng, J. Geiger, L. Giannone, G. Grieger, P. Grigull, H.-J. Hartfuß, D. Hartmann, R. Jaenicke, R. Knig, H. P. Laqua, H. Maaßberg, K. McCormick, F. Sardei, E. Speth, U. Stroth, F. Wagner, A. Weller, A. Werner, H. Wobig, S. Z. and, Major results from the stellarator wendelstein 7-AS, Plasma Physics and Controlled Fusion 50 (5) (2008) 053001. doi:10.1088/0741-3335/50/5/053001.
URL https://doi.org/10.1088%2F0741-3335%2F50%2F5%2F053001

[12] T. S. Pedersen, T. Andreeva, H.-S. Bosch, S. Bozhenkov, F. Effenberg, M. Endler, Y. Feng, D. Gates, J. Geiger, D. Hartmann, H. Hlbe, M. Jakubowski, R. Knig, H. Laqua, S. Lazerson, M. Otte, M. Preynas, O. Schmitz, T. Stange, Y. T. and, Plans for the first plasma operation of wendelstein 7-x, Nuclear Fusion 55 (12) (2015) 126001. doi:10.1088/0029-5515/55/12/126001.
URL https://doi.org/10.1088%2F0029-5515%2F55%2F12%2F126001

[13] S. Bozhenkov, M. Jakubowski, H. Niemann, S. Lazerson, G. Wurden, C. Biedermann, G. Kocsis, R. Knig, F. Pisano, L. Stephey, T. Szepesi, U. Wenzel, T. Pedersen, R. W. and, Effect of error field correction coils on w7-x limiter loads, Nuclear Fusion 57 (12) (2017) 126030. doi:10.1088/1741-4326/aa85ce.
URL https://doi.org/10.1088%2F1741-4326%2Faa85ce

[14] T. Sunn Pedersen, T. Andreeva, H.-S. Bosch, S. Bozhenkov, F. Effenberg, M. Endler, Y. Feng, D. Gates, J. Geiger, D. Hartmann, H. Hölbe, M. Jakubowksi, R. König, H. Laqua, S. Lazerson, M. Otte, M. Preynas, O. Schmitz, T. Stange, Y. Turkin, W7-X Team, Plans for first plasma operation on Wendelstein 7-X, Nuclear Fusion 55.

[15] S. Bozhenkov, F. Effenberg, Y. Feng, J. Geiger, D. Hartmann, H. Hölbe, T. Pedersen, R. Wolf, Limiter for the early operation phase of W7-X, 41st EPS Conf. on Plasma Physics **38F**, P-1.080.

[16] M. Krychowiak, A. Adnan, A. Alonso, T. Andreeva, J. Baldzuhn, T. Barbui, M. Beurskens, W. Biel, C. Biedermann, B. D. Blackwell, H. S. Bosch, S. Bozhenkov, R. Brakel, T. Bräuer, B. Brotas de Carvalho, R. Burhenn, B. Buttenschön, A. Cappa, G. Cseh, A. Czarnecka, A. Dinklage, P. Drews, A. Dzikowicka, F. Effenberg, M. Endler, V. Erckmann, T. Estrada, O. Ford, T. Fornal, H. Frerichs, G. Fuchert, J. Geiger, O. Grulke, J. H. Harris, H. J. Hartfu, D. Hartmann, D. Hathiramani, M. Hirsch, U. Hfel, S. Jaboski, M. W. Jakubowski, J. Kaczmarczyk, T. Klinger, S. Klose, J. Knauer, G. Kocsis, R. König, P. Kornejew, A. Krämer-Flecken, N. Krawczyk, T. Kremeyer, I. Ksiek, A. Kubkowska, M. Langenberg, H. P. Laqua, M. Laux, S. Lazerson,

Y. Liang, S. C. Liu, A. Lorenz, A. O. Marchuk, S. Marsen, V. Moncada, D. Naujoks, H. Neilson, O. Neubauer, U. Neuner, H. Niemann, J. W. Oosterbeek, M. Otte, N. Pablant, E. Pasch, T. Sunn Pedersen, F. Pisano, K. Rahbarnia, L. Ry, O. Schmitz, S. Schmuck, W. Schneider, T. Schrder, H. Schuhmacher, B. Schweer, B. Standley, T. Stange, L. Stephey, J. Svensson, T. Szabolics, T. Szepesi, H. Thomsen, J.-M. Travere, H. Trimino Mora, H. Tsuchiya, G. M. Weir, U. Wenzel, A. Werner, B. Wiegel, T. Windisch, R. Wolf, G. A. Wurden, D. Zhang, A. Zimbal, S. Zoletnik, W7-X Team, Overview of diagnostic performance and results for the first operation phase in Wendelstein 7-X, Rev. Sci. Instrument 87 (2016) 11D304.

[17] D. Wassilew, U. Hoffmann, D. Hildebrandt, Development of an IR-Microbolometer-Camera for Operation in a Strong Magnetic Field, SENSOR+TEST Conferences 2011 Proceedings IRS (2011) IP4.

[18] R. König, J. Baldzuhn, W. Biel, C. Biedermann, R. Burhenn, S. Bozhenkov, J. Cantarini, H. Dreier, M. Endler, H.-J. Hartfuss, D. Hildebrandt, M. Hirsch, M. Jakubowski, R. Jimenez-Gomez, G. Kocsis, P. Kornejev, M. Krychowiak, H. P. Laqua, M. Laux, J. W. Oosterbeek, E. Pasch, T. Richert, W. Schneider, B. Schweer, J. Svensson, H. Thomsen, A. Weller, A. Werner, R. Wolf, D. Zhang, S. Zoletnik, Diagnostics design for steady-state operation of the Wendelstein 7-X stellarator, Rev. Sci. Instrument 81 (2010) 10E133.

[19] H. Niemann, M. Jakubowksi, T. Sunn Pedersen, R. König, G. A. Wurden, F. Effenberg, D. Zhang, W7-X Team, Power loads in the limiter phase of Wendelstein 7-X, 43rd EPS Conf. on Plasma Physics (2016) P4.005.

[20] M. Jakubowski, P. Drewelow, J. Fellinger, A. Puig Sitjes, G. Wurden, A. Ali, C. Biedermann, B. Cannas, D. Chauvin, M. Gamradt, H. Greve, Y. Gao, D. Hathiramani, R. König, A. Lorenz, V. Moncada, H. Niemann, T. T.Ngo, F. Pisano, T. Sunn Pedersen, Infrared Imaging Systems for wall protection in the W7-X stellarator, Review of Scientific Instruments 89 (2018) 10E116–9.

[21] F. Pisano, B. Cannas, M. Jakubowski, H. Niemann, A. Puig Sijtes, G. Wurden, W7-X Team, Towards a new VIS/IR image processing system at W7-X: from spatial calibration to characterization of thermal events, submitted to Review of Scientific Instruments.

[22] V. R. Winters, S. Brezinsek, F. Effenberg, M. Rasinski, O. Schmitz, L. Stephey, C. Biedermann, C. P. Dhard, H. Frerichs, J. Harris, M. Krychowiak, R. König, T. Sunn Pedersen, G. A. Wurden, W7-X Team, Overview of plasma-surface interaction analyses in the limiter phase of W7-X", Physica Scripta T170 (2017) 014050.

[23] G. A. Wurden, C. Biedermann, F. Effenberg, M. Jakubowski, H. Niemann, L. Stephey, S. Bozhenkov, S. Brezinsek, J. Fellinger, B. Cannas, F. Pisano, S. Marsen, H. Laqua, R. Knig, O. Schmitz, J. Harris, E. Unterberg, W7-X Team, Limiter observations during W7-X first plasmas, Nuclear Fusion 57 (2017) 056036.

[24] A. Herrmann, Limitations for divertor heat flux calculations of fast events in tokamaks, EPS 25A.

[25] B. Sieglin, M. Faitsch, A. Herrmann, B. Brucker, T. Eich, L. Kammerloher, S. Martinov, Real time capable infrared thermography for ASDEX Upgrade, REVIEW OF SCIENTIFIC INSTRUMENTS 86 (2015) 113502.

[26] F. Effenberg, Y. Feng, O. Schmitz, H. Frerichs, S. Bozhenkov, H. Hölbe, R. Köenig, M. Krychowiak, T. Sunn Pedersen, D. Reiter, L. Stephey, W7-X Team, Numerical investigation of plasma edge transport and limiter heat fluxes in Wendelstein 7-X startup plasmas with EMC3-EIRENE, Nuclear Fusion 57 (2017) 036021.

[27] S. Bozhenkov, J. Geiger, M. Grahl, J. Kilinger, A. Werner, R. Wolf, Service oriented architecture for scientific analysis at W7-X. An example of a field line tracer, Fusion Engineering and Design 88 (2013) 29973006.

[28] S. Klose, S. Freundt, D. Hathiramani, M. Laux, M. Endler, B. Blackwell, R. König, T. S. Pedersen, the W7-X Team", Design and results of the limiter langmuir probe diagnostics of w7-x, 43rd EPS Conf. on Plasma Physics (2016) P4.005Poster.

[29] T. Wauters, R. Brakel, S. Brezinsek, A. Dinklage, A. Goriaev, H. Laqua, S. Marsen, D. Moseev, T. Stange, G. Schlisio, T. S. Pedersen, O. Volzke, U. W. and, Wall conditioning by ECRH discharges and he-GDC in the limiter phase of wendelstein 7-x, Nuclear Fusion 58 (6) (2018)

066013. doi:10.1088/1741-4326/aab2c9.
URL https://doi.org/10.1088%2F1741-4326%2Faab2c9

[30] T. Stange, H. P. Laqua, M. Beurskens, H.-S. Bosch, S. Bozhenkov, R. Brakel, H. Braune, K. J. Brunner, A. Cappa, A. Dinklage, V. Erckmann, G. Fuchert, G. Gantenbein, F. Gellert, O. Grulke, D. Hartmann, M. Hirsch, U. Höfel, W. Kasparek, J. Knauer, A. Langenberg, S. Marsen, N. Marushchenko, D. Moseev, N. Pablant, E. Pasch, K. Rahbarnia, H. Trimino Mora, T. Tsujimura, Y. Turkin, T. Wauters, R. Wolf, W7-X-Team, Advanced electron cyclotron heating and current drive experiments on the stellarator Wendelstein 7-X, EPJ Web Conf. 157 (02008). doi:https://doi.org/10.1051/epjconf/201715702008.

[31] E. Pasch, M. Beurskens, S. Bozhenkov, G. Fuchert, J. Knauer, R. WOlf, W7-X-Team, The Thomson scattering system at Wendelstein 7-X, Review of Scientific Instruments 87 (11E729). doi:https://doi.org/10.1063/1.4962248.

[32] A. Langenberg, N. A. Pablant, T. Wegner, P. Traverso, O. Marchuk, T. Bruer, B. Geiger, G. Fuchert, S. Bozhenkov, E. Pasch, O. Grulke, F. Kunkel, C. Killer, D. Nicolai, G. Satheeswaran, K. P. Hollfeld, B. Schweer, T. Krings, P. Drews, G. Offermanns, A. Pavone, J. Svensson, J. A. Alonso, R. Burhenn, R. C. Wolf, Prospects of x-ray imaging spectrometers for impurity transport: Recent results from the stellarator wendelstein 7-x (invited), Review of Scientific Instruments 89 (10) (2018) 10G101. doi:10.1063/1.5036536.

[33] A. Langenberg, J. Svensson, H. Thomsen, O. Marchuk, N. A. Pablant, R. Burhenn, R. C. Wolf, Forward Modeling of X-Ray Imaging Crystal Spectrometers Within the Minerva Bayesian Analysis Framework, Fusions Science and Technology 69 (2016) 560–567. doi:https://doi.org/10.13182/FST15-181.

[34] K. Rahbarnia, H. Thomsen, U. Neuner, J. Schilling, J. Geiger, G. Fuchert, T. Andreeva, M. Endler, D. Hathiramani, T. Bluhm, M. Zilker, B. Carvalho, A. Werner, W7-X-Team, Diamagnetic energy measurement during the first operational phase at the Wendelstein 7-X stellarator, Nuclear Fusion 58 (9). doi:https://doi.org/10.13182/FST15-181.

[35] J. Horacek, R. A. Pitts, J. Adamek, G. Arnoux, J.-G. Bak, S. Brezinsek, M. Dimitrova, R. J. Goldston, J. P. Gunn, J. Havlicek, S.-H. Hong, F. Janky, B. LaBombard, S. Marsen, G. Maddaluno, L. Nie, V. Pericoli, T. Popov, R. Panek, D. Rudakov, J. Seidl, D. S. Seo, M. Shimada, C. Silva, P. C. Stangeby, B. Viola, P. Vondracek, H. Wang, G. S. Xu, Y. X. and, Multi-machine scaling of the main SOL parallel heat flux width in tokamak limiter plasmas, Plasma Physics and Controlled Fusion 58 (7) (2016) 074005. doi:10.1088/0741-3335/58/7/074005.
URL https://doi.org/10.1088%2F0741-3335%2F58%2F7%2F074005